Maturation of the functional mouse CRES amyloid from globular form

Aveline Hewetson[a,1], Nazmul H. Khan[b,1], Matthew J. Dominguez[c], Hoa Quynh Do[a], R. E. Kusko[a], Collin G. Borcik[b], Daniel J. Rigden[d], Ronan M. Keegan[d,e], R. Bryan Sutton[c,f], Michael P. Latham[b,f,2], Benjamin J. Wylie[b,f,2], and Gail A. Cornwall[a,2]

[a]Department of Cell Biology and Biochemistry, Texas Tech University Health Sciences Center, Lubbock, TX 79430; [b]Department of Chemistry and Biochemistry, Texas Tech University, Lubbock, TX 79409; [c]Department of Cell Physiology and Molecular Biophysics, Texas Tech University Health Sciences Center, Lubbock, TX 79430; [d]Institute of Integrative Biology, University of Liverpool, L69 7ZB Liverpool, United Kingdom; [e]Science and Technology Facilities Council, Rutherford Appleton Laboratory, OX11 0QX Oxfordshire, United Kingdom; and [f]Center for Membrane Protein Research, Texas Tech University Health Sciences Center, Lubbock, TX 79430

Edited by Christopher P. Jaroniec, The Ohio State University, Columbus, OH, and accepted by Editorial Board Member Michael F. Summers May 7, 2020 (received for review April 14, 2020)

The epididymal lumen contains a complex cystatin-rich nonpathological amyloid matrix with putative roles in sperm maturation and sperm protection. Given our growing understanding for the biological function of this and other functional amyloids, the problem still remains: how functional amyloids assemble including their initial transition to early oligomeric forms. To examine this, we developed a protocol for the purification of nondenatured mouse CRES, a component of the epididymal amyloid matrix, allowing us to examine its assembly to amyloid under conditions that may mimic those in vivo. Herein we use X-ray crystallography, solution-state NMR, and solid-state NMR to follow at the atomic level the assembly of the CRES amyloidogenic precursor as it progressed from monomeric folded protein to an advanced amyloid. We show the CRES monomer has a typical cystatin fold that assembles into highly branched amyloid matrices, comparable to those in vivo, by forming β-sheet assemblies that our data suggest occur via two distinct mechanisms: a unique conformational switch of a highly flexible disulfide-anchored loop to a rigid β-strand and by traditional cystatin domain swapping. Our results provide key insight into our understanding of functional amyloid assembly by revealing the earliest structural transitions from monomer to oligomer and by showing that some functional amyloid structures may be built by multiple and distinctive assembly mechanisms.

cystatin | amyloid | X-ray crystallography | NMR spectroscopy

Amyloids, including fibrils, films, and matrices, are formed by the self-association of proteins into higher ordered cross β-sheet structures. Although traditionally viewed solely as pathological oligomers or plaques integral to neurodegenerative diseases and prionopathies, a growing body of evidence now suggests that many proteins form amyloid which perform important biological roles. These functional amyloids have been implicated in processes including melanin synthesis; germline specification; formation of long-term memory; sperm maturation, clearance, and fertilization; and hormone storage (1–8). Functional amyloids follow similar aggregation pathways as pathological forms, assembling from monomer to intermediate oligomers to advanced amyloids. Despite forming similar structures, functional amyloids are distinct from pathological forms since they are produced in vivo without significant cytotoxicity and often reversibly disassemble (6, 8, 9). Further, some functional amyloids are elaborate structures composed of multiple amyloidogenic precursors adding another level of complexity to their assembly (6, 7, 10). However, the mechanism(s) by which functional amyloids assemble and disassemble is poorly understood. This lack of knowledge is due, in part, to the difficulty in purifying amyloidogenic precursors under nondenaturing conditions which would then allow for examination of the structural transitions required for the assembly of amyloid from natively folded protein. Indeed, although structural biology techniques including cryogenic electron microscopy (cryoEM) and NMR spectroscopy have revealed atomic resolution of protofibrils and highly ordered amyloid fibrils, this work has primarily focused on pathological amyloids such as Aβ and/or discrete amyloidogenic domains (11–17). Elucidation of the structural and dynamic transitions of whole amyloidogenic precursors along their assembly pathway is therefore needed to reveal possible mechanisms that initiate and control amyloidogenesis and to identify differences between functional and pathogenic amyloid assembly and structure.

In previous studies, we demonstrated that a nonpathological amyloid matrix with proposed roles in sperm maturation and sperm protection is present throughout the normal mouse epididymal lumen (4). Further, the amyloid matrix changes along the length of the epididymal tubule transitioning from an anti-A11 immunoreactive amyloid composed of matrices and films in the proximal

Significance

Some amyloids are functional in the normal physiology of cells. Of these, several have been found in complex amyloid matrices that are composed of multiple amyloidogenic precursors. Here we trace the lifecycle of the mouse CRES (cystatin-related epididymal spermatogenic) protein, a functional amyloidogenic precursor and component of a complex amyloid matrix in the epididymis, as it progresses from monomeric folded protein to an advanced amyloid. We discovered that CRES amyloid formation may involve β-sheet assemblies generated by two distinct mechanisms: those formed by a flexible CRES loop and those formed by domain swapping. These mechanisms would provide multiple contact surfaces for further β-sheet assemblies with neighboring proteins resulting in sophisticated quaternary structures which may be integral for biological function.

Author contributions: R.B.S., M.P.L., B.J.W., and G.A.C. designed research; A.H., N.H.K., M.J.D., H.Q.D., R.E.K., R.B.S., M.P.L., B.J.W., and G.A.C. performed research; M.J.D., H.Q.D., R.E.K., C.G.B., D.J.R., R.M.K., R.B.S., M.P.L., B.J.W., and G.A.C. analyzed data; and N.H.K., R.B.S., M.P.L., B.J.W., and G.A.C. wrote the paper.

The authors declare no competing interest.

This article is a PNAS Direct Submission. C.P.J. is a guest editor invited by the Editorial Board.

Data deposition: The atomic coordinates and structure factors have been deposited in the Protein Data Bank, PDB ID code 6UIO. NMR data have been deposited in the Biological Magnetic Resonance Bank (solution-state ID 50273 and solid-state ID 50275).

[1]A.H. and N.H.K. contributed equally to this work.

[2]To whom correspondence may be addressed. Email: michael.latham@ttu.edu, benjamin.j.wylie@ttu.edu, or gail.cornwall@ttuhsc.edu.

This article contains supporting information online at https://www.pnas.org/lookup/suppl/doi:10.1073/pnas.2006887117/-/DCSupplemental.

First published June 29, 2020.

epididymis to one rich in fibrils in the distal epididymis (18). The epididymal amyloid matrix contains several family 2 cystatins of cysteine protease inhibitors, including cystatin C and four members of the CRES (cystatin-related epididymal spermatogenic) subgroup, a reproductive subgroup of family 2 cystatins (10). We further showed the amyloid forms of CRES subgroup members are present in the epididymal amyloid matrix and their recombinant forms readily form amyloid in vitro (10). These results suggest CRES subgroup members are functional amyloidogenic precursors that together contribute to the formation of a complex extracellular amyloid structure.

To determine how a functional amyloidogenic precursor assembles into amyloid, we previously showed that native CRES assembled from a monomer with mixed secondary structure into a metastable antiparallel β-sheet rich oligomer, that eventually assembled into a higher-ordered amyloid (19). In the present study we now follow the assembly of CRES from monomer to amyloid at the atomic level. We used X-ray crystallography and solution-state NMR to determine the structure and dynamics of the CRES monomer and its earliest oligomeric forms. Solid-state NMR (ssNMR) then revealed structural details of the advanced CRES amyloid. Together, our data suggest that CRES amyloid assembly occurs by two distinct mechanisms which may allow the controlled formation of complex quaternary structures, including highly branched amyloid matrices, that are characteristic of the functional amyloid structure in the lumen of the proximal mouse epididymis.

Results and Discussion

Crystal Structure of CRES Reveals a Monomeric Cystatin Fold. Mature mouse CRES lacking the signal sequence (residues 1 to 19) was modified with a cysteine 48 to alanine mutation (C48A) to prevent inappropriate disulfide bond formation. The crystallization experiments were carried out using the hanging-drop vapor-diffusion method, and diffraction quality crystals were obtained after 6 mo via a robotic screen using Molecular Dimensions screening conditions. Crystals of CRES C48A were grown in 2.1 M ammonium sulfate, 0.2 M Na iodide, pH 5.8 at 10 °C. The crystals were in space group $P2_12_12_1$ and diffracted to 1.8-Å resolution. We modeled 22 iodide (I^-) and 2 molecular iodine (I_2) ligands in the structure. The iodine positions were confirmed by anomalous difference maps. Although we were unable to solve the structure with traditional replacement techniques using the stabilized cystatin C monomeric structure (3GAX) (20), we were able to compute a partial solution using AMPLE (21). AMPLE was able to place a significantly trimmed ensemble of eight distantly homologous cystatin-fold structures. Interestingly, we were able to solve the CRES structure using the recently published crystal structure of V57G mutant of human cystatin C (6ROA) (22). There were four CRES molecules in the asymmetric unit. The crystallographic data are summarized in *SI Appendix*, Table S1.

The CRES C48A structure is shown in Fig. 1*A*. The overall structural similarity of CRES to other family 2 cystatins was high, as expected, as the primary sequence alignment between cystatin C and CRES is 47.6% similar (24% identical). However, unlike other wild-type cystatins which crystallized as domain swapped dimers, CRES C48A remained a monomer and exhibited a typical cystatin fold characterized by an unstructured N terminus leading into a long α-helix sitting atop a five-stranded antiparallel β-sheet. Similar to crystal structures of other cystatins, no electron density was observed for the first 11 N-terminal residues (22). In cystatin C this is thought to be due to the inherent flexibility of the N-terminal region (23). Matrix-assisted laser desorption/ionization (MALDI) mass spectrometry analysis of C48A CRES, however, revealed two populations with masses of 14764.63 and 12978.78 Da, suggesting a proportion of CRES was processed during purification. Tryptic digests indicated that the first 11 residues from the N terminus were missing from the smaller CRES C48A protein (*SI Appendix*, Fig. S1). Although the mechanism by which this processing occurred is unknown, the N-terminal truncation of CRES may help initiate its aggregation. Indeed, the loss of the first 10 to 11 N-terminal amino acids is a characteristic of several family 2 cystatins and, as shown for cystatin C and cystatin E, facilitated their self-assembly (22, 24–26). Both 14-kDa and 12-kDa CRES forms are present in the mouse epididymal lumen, suggesting the N-terminal processing

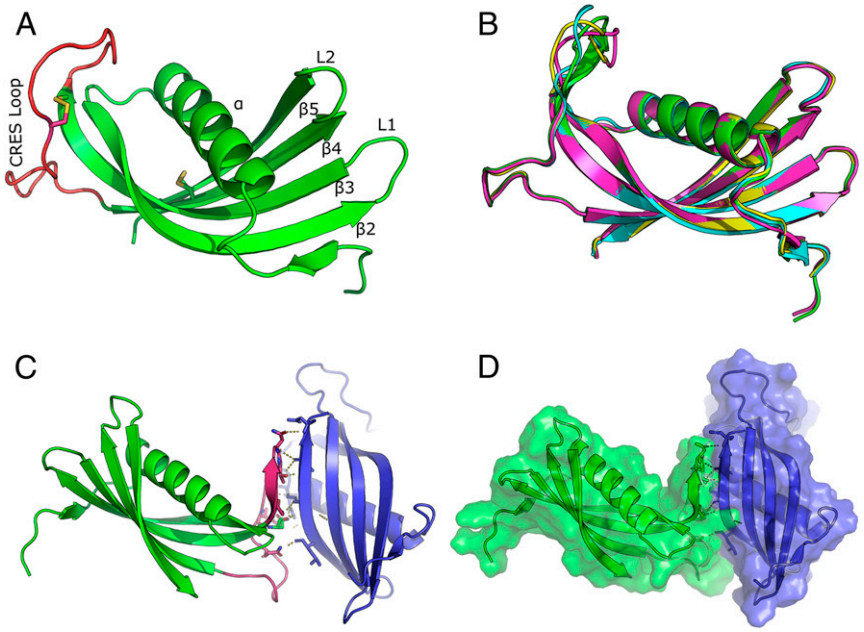

Fig. 1. X-ray crystal structure of CRES. (*A*) Ribbon diagram of the CRES monomer highlighting the CRES loop in red and the two disulfide bonds as yellow sticks. (*B*) Superposition of the four CRES molecules in the crystallographic asymmetric unit (PDB code 6UIO) (55). (*C*) Intermolecular interaction of two CRES molecules in the crystallographic asymmetric unit. Highlighted in pink is the CRES loop and β3 of one molecule forming a parallel β-sheet interaction with β5 of an adjacent molecule. (*D*) Space-filling model of the two interacting CRES molecules.

of CRES is biologically relevant (4). The electron density of all four CRES molecules in the asymmetric unit began after the cleavage site, suggesting only N-terminally truncated molecules in the crystal.

Like other family 2 cystatins, CRES C48A contained two defined loop structures, L1 which connects β-strands 2 and 3 and L2 which connects β-strands 4 and 5 (Fig. 1*A*). Although L1 and L2 contribute to the papain (C1 cysteine protease) binding site in typical family 2 cystatin monomers, CRES does not inhibit papain in vitro, likely due to the lack of the highly conserved Q-X-V-X-G site for inhibition (27). Notably, CRES C48A contains a threonine (Thr) instead of a valine (Val) residue at this position in L1 (...QITDR...). In cystatin C the conformational strain around Val-57 in L1 creates a hinge within the loop that causes it to domain swap. In fact, mutating this residue to asparagine (N) or glycine (G) resulted in monomeric cystatin C (22, 25). The absence of this critical residue in L1 may be why CRES C48A did not undergo domain swapping during crystallization. Indeed, Val has the lowest probability of being in a β-turn, hence the structural instability, while Thr has an average probability (28). The electron density in the CRES L1 loop shows that the Thr-79 in L1 is well ordered (*SI Appendix*, Fig. S2). While the φ-ψ angles of Thr-79 map to a similar region of Ramachandran space as Val-57 in cystatin C, the backbone angles for Thr-79 in CRES are not technically forbidden (*SI Appendix*, Fig. S2). However, this site in CRES, like other cystatins, is likely structurally strained for similar reasons.

An Interaction in the Crystal Structure Suggests a Path to Amyloid. Opposite to the papain inhibitory region in the CRES C48A monomer is a disordered disulfide-anchored loop connecting β3 and β4, which we refer to as the CRES loop (Fig. 1*A*). This disordered region is also present in other cystatins and has been called an "appending structure" (AS) or legumain exosite loop (LEL) because of its interaction with the C13 cysteine protease legumain (25, 26). It is not known if CRES, like cystatins C, E, and F, inhibits legumain. An overlay of the four CRES C48A molecules in the asymmetric unit showed the only variability between the four molecules was in the flexible CRES loop (Fig. 1*B*). Unexpectedly, CRES molecules A and B interacted with each other via an asparagine-rich region of the CRES loop of molecule A and the main chain atoms along β-strand 5 of molecule B, forming what may be an extended pseudo parallel β-sheet interaction (Fig. 1*C* and *SI Appendix*, Fig. S3). In fact, dictionary of protein secondary structure (DSSP), which computes secondary structure, made the CRES loop into an elongated β-strand 3 of chain A upon contact with β-strand 5 of CRES chain B (29). The parallel β-strand formed by the interaction between the two molecules was held together by two salt bridges and eight H-bonds with distances typical of those present in β-sheet interactions (*SI Appendix*, Fig. S3 and Table S2). The interface formed between these two molecules buried ∼1295 Å^2 as measured using PISA (30), suggesting a biologically meaningful interaction (Fig. 1*D*). This interaction could represent an early assembly state of CRES as it transitions to a higher ordered amyloid via a mechanism other than that of domain swapping.

Solution-State NMR Confirms the Cystatin Fold of CRES. To better understand the transition of the cystatin C-like CRES structure observed in the crystal to the form found in the amyloid, we turned to solution-state NMR. Uniformly ^{13}C and ^{15}N-labeled CRES C48A in 25 mM 2-(4-morpholino)-ethane sulfonic acid (MES), 250 mM NaCl, 1 mM ethylenediaminetetraacetic acid (EDTA) buffer, pH 6 was used for standard triple-resonance backbone assignment experiments that were performed immediately following protein purification (Fig. 2*A*) (56). We previously showed by dynamic light scattering that, under these buffer conditions, the majority of particles were of a size expected for a CRES monomer with occasionally slightly larger particles detected (19). Torsion angle likelihood obtained from shift-neural network (TALOS-N) was then used to calculate secondary structure propensities from the backbone assignments (31). As shown in Fig. 2*B*, a good agreement was observed between the secondary structural elements observed in the crystal structure and the solution-state NMR data confirming the cystatin C-like fold of CRES C48A in solution. TALOS-N was also used to derive random coil index ^{15}N order parameters (S^2), which are a measure of backbone flexibility (32). A good inverse correlation was observed between the average crystallographic b-factors (Fig. 2*C*, green points) and the predicted ^{15}N S^2 (blue points), where amides with low b-factors have high S^2, indicating a rigid backbone, and amides with high b-factors have low S^2, indicating a flexible backbone (33). We note that several residues (E103 to I106) in the CRES loop connecting the β3 and β4 strands had elevated S^2 values (decreased b-factors), designating decreased motion in this section of the loop in both the crystal and solution states. Chemical shift-ROSETTA (CS-ROSETTA) confirmed nearly the same fold as the crystal structure (*SI Appendix*, Fig. S4).

Monitoring the CRES Transition to Amyloid. To characterize the initial steps of CRES C48A into its early oligomeric amyloid form, we measured solution-state NMR ^{15}N relaxation experiments sensitive to the pico-to-nanosecond and millisecond timescales. Data were initially collected in 25 mM MES, 250 mM NaCl, 1 mM EDTA, pH 6 buffer conditions where we predict CRES is predominantly a monomer. The pH of the buffer was then adjusted to pH 7.5, by the addition of 50 mM Hepes, pH 8, which also reduced the salt concentration to 173 mM, to promote amyloidogenesis (19). Initial comparison of the two-dimensional (2D) ^{15}N,^{1}H heteronuclear single-quantum coherence (HSQC) spectra recorded in the two buffer conditions revealed a series of chemical shift perturbations (CSPs; average of all CSPs = 0.02, *SI Appendix*, Table S3), which are mapped on the structure of CRES C48A in Fig. 3*A*. The largest CSPs upon increasing the pH occurred in strands β2 and β3 and to the adjacent region of α-helix. Notably, the largest CSP involved 73H in strand β2: this perturbation and the neighboring effects likely reflect deprotonation of the imidazole side chain in the histidine residue upon shifting the pH to more basic conditions. In addition to the CSPs highlighted in Fig. 3*A*, several resonances in the CRES loop (99L, 100N, 101N, 102T, and 104N) experience extreme line broadening and are undetectable upon shifting the pH to 7.5. A set of peaks in the homologous region were also missing in the NMR data for monomeric V57G cystatin C mutant, which was collected at pH 7.4 and 50 mM NaCl (22). This commonality suggests that the AS structure in cystatin C, which is equivalent to the CRES loop here, also changes structure under physiological conditions. The disappearance of peaks in an HSQC spectrum, as seen here, is indicative of "intermediate" conformational exchange on the millisecond timescale between the observable "ground" state and a lowly and transiently populated excited state. Thus, our ^{15}N,^{1}H HSQC data suggested that motions within CRES, including the flexible CRES loop, are present at physiological pH.

We next compared the difference in the ^{15}N transverse relaxation (R_2) rates from the initial and pH 7.5 high salt conditions (250 vs. 173 mM) (Fig. 3*B*, blue points). The ^{15}N R_2 is predominantly sensitive to the nanosecond timescale of global macromolecular tumbling as well as the amplitude and picosecond timescale of local amide bond motion, although millisecond timescale motions can have an additive effect as well (see below) (34). Therefore, differences in oligomeric state or protein dynamics upon shifting the solution conditions to pH 7.5 could be manifested as a change in ^{15}N R_2 (12). Generally, we observed an average difference in R_2 ($\Delta R_2 = R_{2,\text{initial}} - R_{2,\text{pH 7.5}}$) of −3.22 s^{-1}

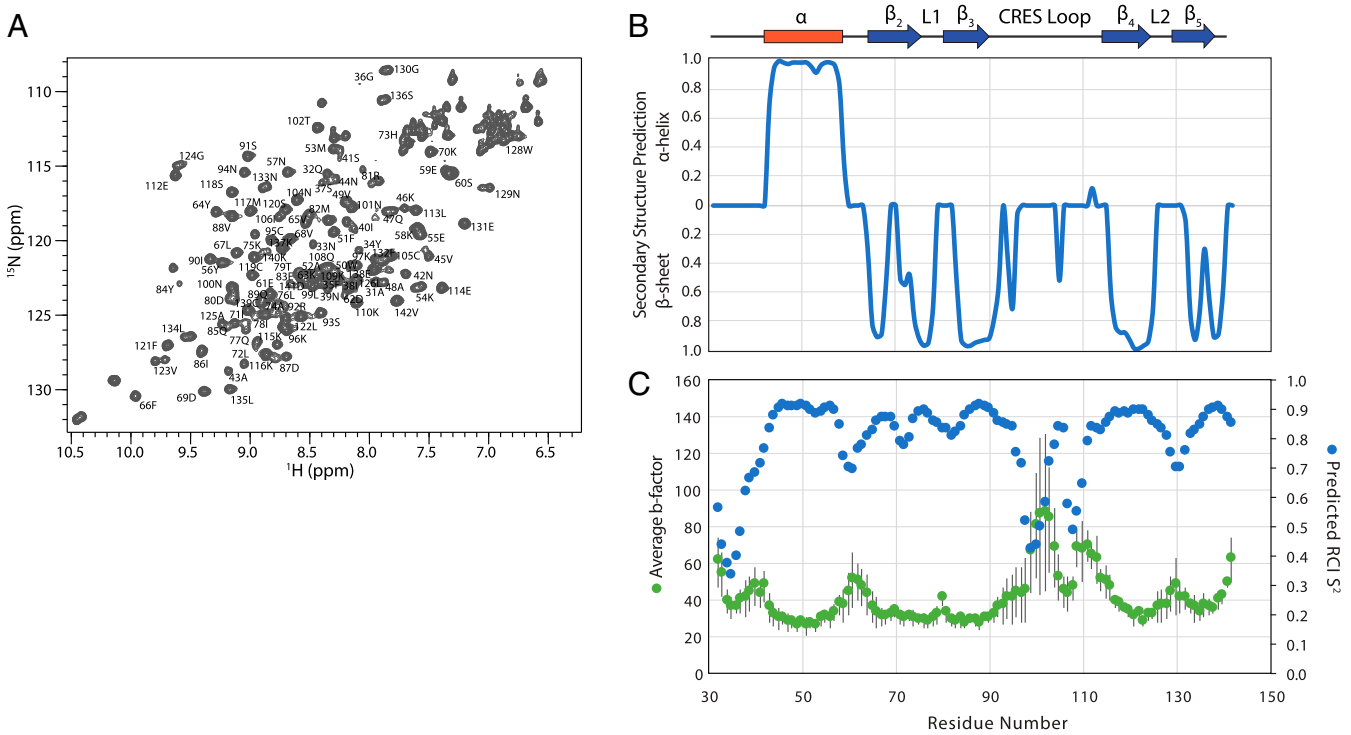

Fig. 2. Solution-state NMR on monomeric CRES. (*A*) Two-dimensional ^{15}N,^{1}H HSQC spectrum of 1.4 mM CRES in 25 mM MES, 250 mM NaCl, 1 mM EDTA, pH 6 at 25 °C. Resonance assignments are given as the residue number and amino acid single letter code. (*B*) Secondary structure propensity of solution-state CRES derived from backbone chemical shifts and TALOS-N. The secondary structure observed in the crystal structure is diagrammed above. (*C*) Comparison of the average b-factors from the four CRES monomers in the crystallographic asymmetric unit (green points) and the predicted random coil index (RCI) order parameter (S^2) (blue points), which were also calculated from the backbone chemical shifts using TALOS-N. The SDs of the crystallographic b-factors of the four monomers are given as gray error bars.

(blue dashed line in Fig. 3*B*). Although a reason for this difference could be from overall rigidification and/or slower tumbling of the observed CRES (see *SI Appendix*), another explanation for the larger R_2 values at pH 7.5 is that monomeric CRES is rapidly exchanging with a much larger oligomeric form of CRES, which would have much larger R_2 rates. If this exchange process is faster than R_2, then $R_{2,\text{pH 7.5}}$ would be the population weighted average of the rates from the monomeric and oligomeric forms (12). We hypothesize that this larger tumbling time was the result of the early stages of amyloidogenesis with CRES C48A subunits associating—either stably or transiently. We also observed larger differences in ΔR_2 (both positive and negative) for several residues (Fig. 3*B*). These ΔR_2 values likely reflect changes in amide dynamics that accompany differences in structure.

We also collected ^{15}N Carr-Purcell-Meiboom-Gill (CPMG) relaxation dispersion experiments, which are a powerful method to quantify conformational exchange processes that occur on the millisecond timescale. Transitions to these lowly populated "excited" states are important for a range of biological functions including enzyme catalysis and protein folding (35). Under the initial buffer conditions, CRES displayed flat dispersion curves indicating that an exchange process on this timescale is not present (Fig. 3*C*, black points). However, when the solution conditions were shifted to pH 7.5, typical dispersion curves, with $R_{2,\text{eff}}$ decreasing with increasing ν_{CPMG} as shown in Fig. 3*C* (blue points), were obtained. These profiles were only observed for residues Q77 to M82 and A125, L126, N129, E131, and F132, which are in the L1 and L2 loops, respectively. Since these residues have little or no CSPs upon switching to the low salt buffer and are on the other side of the protein from the CRES loop residues that experience extreme line broadening, we suggest that this exchange phenomenon is separate from the process(es) causing CSP, line broadening, and the observed ΔR_2. Relaxation dispersion data collected at one static magnetic field strength, corresponding to ^{1}H field of 600 MHz, were fit to a global two-site exchange model to derive $k_{ex} = 840 \pm 180\ s^{-1}$ and $p_b = 1.2\% \pm 0.2\%$ (*SI Appendix*, Table S4). Together, the comparison of solution-state NMR data at 250 mM NaCl and pH 6, where CRES exists as a stable monomer, and 173 mM NaCl and pH 7.5, which may promote the earliest stages of amyloidogenesis, suggests that the initial steps of amyloid formation are characterized by changes in the structure and dynamics of the α-helix, the CRES loop connecting strands β3 and β4, and the opposing edge of the β-sheet (i.e., L1 and L2).

We next sought to drive the formation of CRES amyloid further; therefore, we prepared a ^{15}N-labeled CRES sample in no salt and pH 7.5 buffer, which we have previously shown rapidly accelerates the formation of CRES oligomers (19), and measured the same suite of ^{15}N relaxation experiments. Initial characterization of the ^{15}N,^{1}H HSQC spectra (Fig. 3*A*) revealed that, in addition to the CSPs observed upon shifting the pH to 7.5 and 173 mM NaCl, more perturbations occurred when salt was omitted from the buffer (average of all CSPs = 0.04, *SI Appendix*, Table S3). These CSPs now include the majority of the residues in CRES, including perturbations in the β-sheet. Notably, peaks in the CRES loop between strands β3 and β4 were still missing under these conditions (residues L99, N100, N101, and N104), indicating that the millisecond timescale dynamics observed at 173 mM NaCl for this region of the protein were still present in the no salt buffer condition. We next compared the ^{15}N R_2 relaxation rates of the amide groups under the original and pH 7.5/no salt buffer conditions (Fig. 3*B*, red points). Again, a generally uniform decrease in the R_2 rates were observed with an average ΔR_2 ($R_{2,\text{initial}} - R_{2,\text{pH 7.5/no salt}}$; red dashed line in

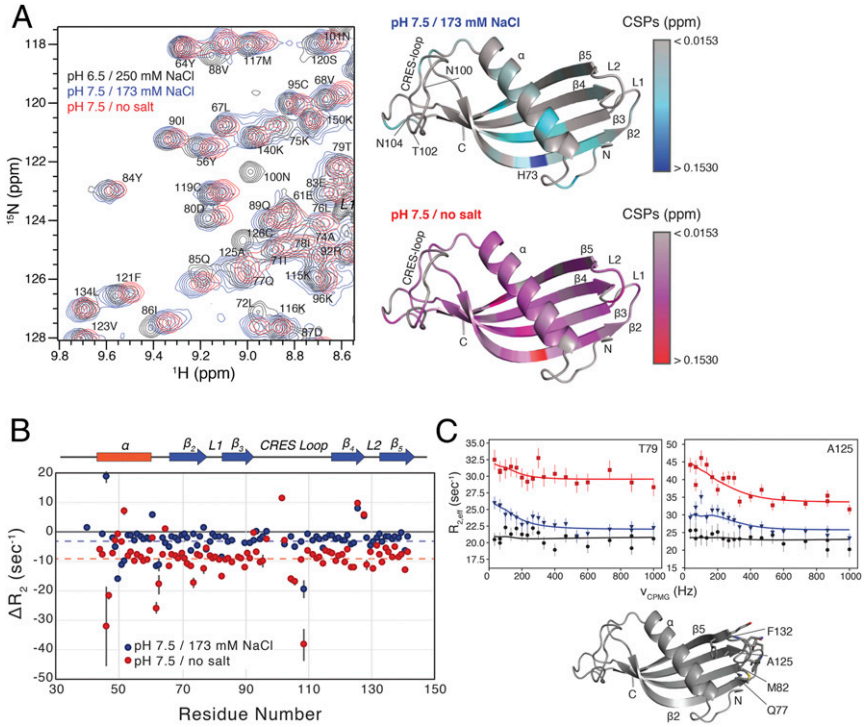

Fig. 3. Changes in the structure and dynamics of CRES upon amyloidogenesis. (*A*, *Left*) Overlay of a region from the 2D ^{15}N,^{1}H HSQC spectra of 1.4 mM CRES at pH 6/250 mM NaCl (black contours), pH 7.5/173 mM NaCl (blue contours), and pH 7.5/0 mM NaCl (red contours). (*A*, *Right*) Calculated CSPs mapped onto the crystal structure of CRES. The CSPs between pH 6/250 mM NaCl and pH 7.5/173 mM NaCl are given as a gray-to-blue gradient, and the CSPs between pH 6/250 mM NaCl and pH 7.5/0 mM NaCl are given as a gray-to-red gradient. (*B*) Plot of the ΔR_2 versus residue number. Blue points are the differences between pH 6/250 mM NaCl and pH 7.5/173 mM NaCl, and the red points are the differences between pH 6/250 mM NaCl and pH 7.5/0 mM NaCl. The error in the values, propagated from the covariance matrix of the fits, are shown as gray bars. The blue and red dashed lines highlight the average difference in ΔR_2 for the two conditions. (*C*) Representative relaxation dispersion CPMG profiles are shown for CRES at pH 6/250 mM NaCl (black circles), pH 7.5/173 mM NaCl (blue triangles), and pH 7.5/0 mM NaCl (red squares) collected at 600 MHz and 25 °C. Error bars are derived from duplicate measurements of $R_{2,eff}$ at two CPMG fields. Solid lines are fit to the Bloch-McConnell equations describing two-site exchange. Below the plots, the residues for which chemical exchange phenomenon are observed are shown as sticks on the crystal structure.

Fig. 3*B*) of −9.09 s^{-1}. These data suggest that monomeric CRES is rapidly exchanging with a larger oligomeric form and that this exchange is greater under these conditions (*SI Appendix*). Finally, we also measured ^{15}N relaxation dispersion data on the pH 7.5/no salt sample (Fig. 3*C*, red points). Here, we observed relaxation dispersion profiles in the L2 loop connecting strands β4 and β5 (A125, L126, W128, and G130) and in the L1 loop. Fitting these data to a two-state exchange model resulted in a $k_{ex} = 1{,}220 \pm 290\ s^{-1}$ and $p_b = 3.1\% \pm 0.7\%$ (*SI Appendix*, Table S4), which are consistent with the notion that monomeric CRES is undergoing more exchange in the pH 7.5/no salt buffer condition.

In total, our solution-state NMR relaxation data present a picture of CRES sampling an oligomeric conformation using interactions on either end of the β-sheet (i.e., L1/L2 loops and CRES loop). Although the role of the L1 loop in domain swapping and oligomerization is well established for several cystatins, the flexible CRES loop, that is also present in all family 2 cystatins, has largely been ignored. Interestingly, the intermediate exchange line broadening for CRES loop resonances observed in the HSQC spectra and the CPMG data observed for L1/L2 residues imply that these two mechanisms for amyloidogenesis are distinct and complementary processes, as these two NMR observations could be on different timescales (*SI Appendix*). Thus, our data suggest the CRES loop may also participate in oligomerization but by an assembly mechanism distinct from domain swapping.

ssNMR Chemical Shift Assignments. A sample of ^{15}N, ^{13}C-labeled CRES C48A was sonicated into a stable amyloid form and packed into an ssNMR rotor. This sample formed a complex branched amyloid matrix similar to that in the proximal epididymal lumen (see Fig. 6*D*) (4, 18). As previously reported, β-sheet and random coil ^{13}C chemical shifts dominated the ssNMR spectra of the advanced amyloid state of CRES (19, 57). The abundance of antiparallel β-sheet secondary structure produced significant chemical shift overlap, which was worsened by natural ^{13}C linewidths of 0.5 ppm (75 Hz). These broad lines are likely due, in part, to sample polymorphism as discussed below. To address the issue of peak overlap, in addition to 2D dipole-assisted rotational resonance (DARR; 12-ms, 25-ms, and 50-ms mixing times) and NcaCX and NcoCX spectra, we acquired three-dimensional (3D) CANcoCA ($C\alpha$-N-c'-$C_{\alpha i-1}$), NCACX (N_i-$C\alpha_i$-$C_{i,sidechain}$), and NCOCX (N_i-C'_{i-1}-$C_{i-1,sidechain}$) spectra. The signal to noise of these spectra was improved using double exponential weighted sampling and following protocols we and others previously reported (36, 37). We assigned all backbone ^{15}N and ^{13}C and most sidechain resonances for 112 residues stretching from Q32 through V142, with limited ambiguity. This process required high-resolution processing of datasets to resolve correlations along the backbone, with processing optimized for signal to noise to identify long sidechain spin systems. Proline backbone resonances were confidently assigned using the CANcoCA spectrum. We depict backbone walks through key regions of the protein, including the residues found in the α-helix of the X-ray crystal structure (*SI Appendix*, Fig. S5), L1 loop

region (*SI Appendix*, Fig. S6), CRES loop (*SI Appendix*, Fig. S7), and the C terminus (*SI Appendix*, Fig. S8). The CANcoCA spectrum was essential to identification of unambiguous chemical shift correlations. The completeness of the ssNMR assignments is depicted in an extensively assigned DARR spectrum (Fig. 4 and *SI Appendix*, Fig. S9), strip plots (*SI Appendix*, Figs. S5–S8), and is explicitly illustrated in *SI Appendix*, Fig. S10. All observed cysteine Cβ chemical shifts were indicative of oxidized sidechains, signifying that disulfide bonds formed in the monomeric globular state are preserved throughout amyloidogenesis. The DARR spectra further revealed the relative rigidity of the amyloid structure, as multiple Cα-Cα cross peaks (correlations between nearest neighboring Cα residues) appear at relatively short (25 ms) DARR mixing times, indicating little motional attenuation of ^{13}C-^{13}C through-space couplings. The completeness of our chemical shift assignments allowed us to perform a detailed analysis of the differences between the globular monomeric structure and the amyloid form, as we describe below.

We calculated the changes in Cα and Cβ chemical shifts between solution and solid-state NMR assignments ($CSP = \delta_{C_{solution}} - \delta_{C_{solid}}$, where δ_C is the Cα or Cβ chemical shift in parts per million) to determine the change in local structure (*SI Appendix*, Fig. S11). We observed 34 significant (1.5 ppm) Cα CSPs and mapped the absolute values onto the liquid-state NMR structure (Fig. 5*A*). Among these 34 residues, 14 were located in the α-helix found in the X-ray crystal structure revealing changes in the protein fold. The other 20 Cα CSPs were distributed throughout the rest of the protein but predominated in the L1, L2, and CRES loops. The appearance of multiple CSPs in these loops implied there may be some reorientation of the β-strands in the amyloid complex, while the strands themselves largely retained their original structure. The data further indicate the CRES loop may indeed participate in amyloid assembly because the chemical shifts now appear to have β-sheet secondary structure.

We then calculated the secondary structure of the protein using TALOS-N. This analysis confirmed that the globular β-sheet was largely conserved. However, the dihedral angles predicted from ssNMR chemical shifts deviated substantially in other regions of CRES (Fig. 5*B*) from the secondary structure propensities derived from the liquid-state NMR chemical shifts which were in good agreement with the X-ray crystallographic structure (Fig. 2*B*). Here, we observed dramatic changes for residues A43 to E59, situated in the α-helix of the X-ray crystal structure, the L1 loop, and the CRES loop. TALOS-N predicted the long α-helix transitioned to a β-strand. The L1 loop also shifted toward β-strand secondary structure. As shown in Fig. 5*B*, TALOS-N predicted a continuous β-strand was formed by β-strands 2 and 3 and the L1 loop. This observation is bolstered by the large CSPs observed in the L1 loop, which all shifted toward canonical $^{13}C\alpha$ and $^{13}C\beta$ β-sheet chemical shifts (Fig. 5*A*). The formation of a long β-strand is consistent with domain swapped structures observed in other cystatin proteins (26, 38), thus this observation is not unexpected. Additionally, the chemical shifts also indicate the CRES loop can form two short β-strands. We further established the increased rigidity of the protein by calculating the random coil index S^2 with TALOS-N. The predicted S^2 from solid-state chemical shifts were generally higher compared to the globular form of the protein (Fig. 5*C*). This was especially true for the CRES loop region and the L1 loop, which may coincide with the formation of extended secondary structure.

To further our chemical shift analysis, we used AmylPred2, a web tool which uses the consensus from 11 different methods, to predict the amyloid prone regions of CRES (39). In Fig. 5*A* (*Right*), residues colored in gray have no predicted amyloid propensity, whereas other residues are shaded from green to purple depending upon the number of AmylPred2 predictors that selected that residue as amyloid prone. Four residues found in the α-helix were predicted to be amyloidogenic by all 11 components, and 88 residues overall were picked to have some amyloid propensity. It should be noted that even though AmylPred2 did not predict that residues within the CRES loop were amyloid prone, the shift toward β-sheet secondary structure (Fig. 5*B*) implies that these residues could still play a role in amyloid formation. Together, TALOS-N and AmylPred2 suggest that the α-helix, L1 loop, CRES loop, and multiple regions of the preexisting, preassembled β-strands are pivotal regions for the transition into the amyloid fold. The many amyloid-prone sites found in the β-sheet indicate the CRES amyloid may come partially assembled within the globular protein. This could further help to explain the unusually fast rate (days vs. weeks) of amyloid formation in CRES proteins compared to pathological amyloidogenic proteins. This also could help to explain why previous fourier-transform infrared spectroscopy (FTIR) and circular dichroism (CD) measurements of CRES aggregates exhibited much higher antiparallel vs. parallel β-sheet content, which runs contrary to commonly observed amyloid structures (19). Many of the globularly native intramolecular antiparallel β-sheets are conserved within the amyloid matrix and in turn nucleate intermolecular antiparallel β-sheets.

Determination of a CRES Model and Implications for the Complexity of CRES Amyloid Quaternary Structure. Our experimental chemical shifts strongly suggest β-strands 2 and 3 and the L1 loop form an elongated β-strand within the mature amyloid matrix. This longer β-stand may indicate a domain-swapped structure as observed in

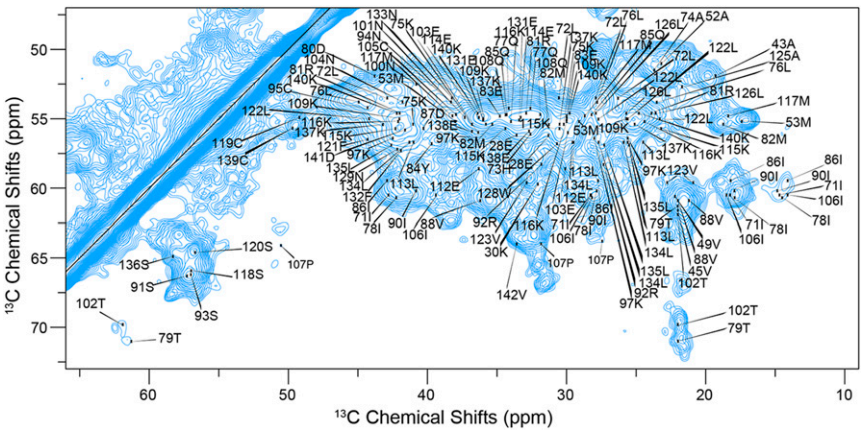

Fig. 4. ssNMR assignments of an advanced amyloid form of CRES. Two-dimensional ^{13}C,^{13}C DARR spectrum of CRES. The spectrum was recorded with a mixing time of 25 ms at a magnetic field of 14 T. All assigned correlations are labeled with residue number.

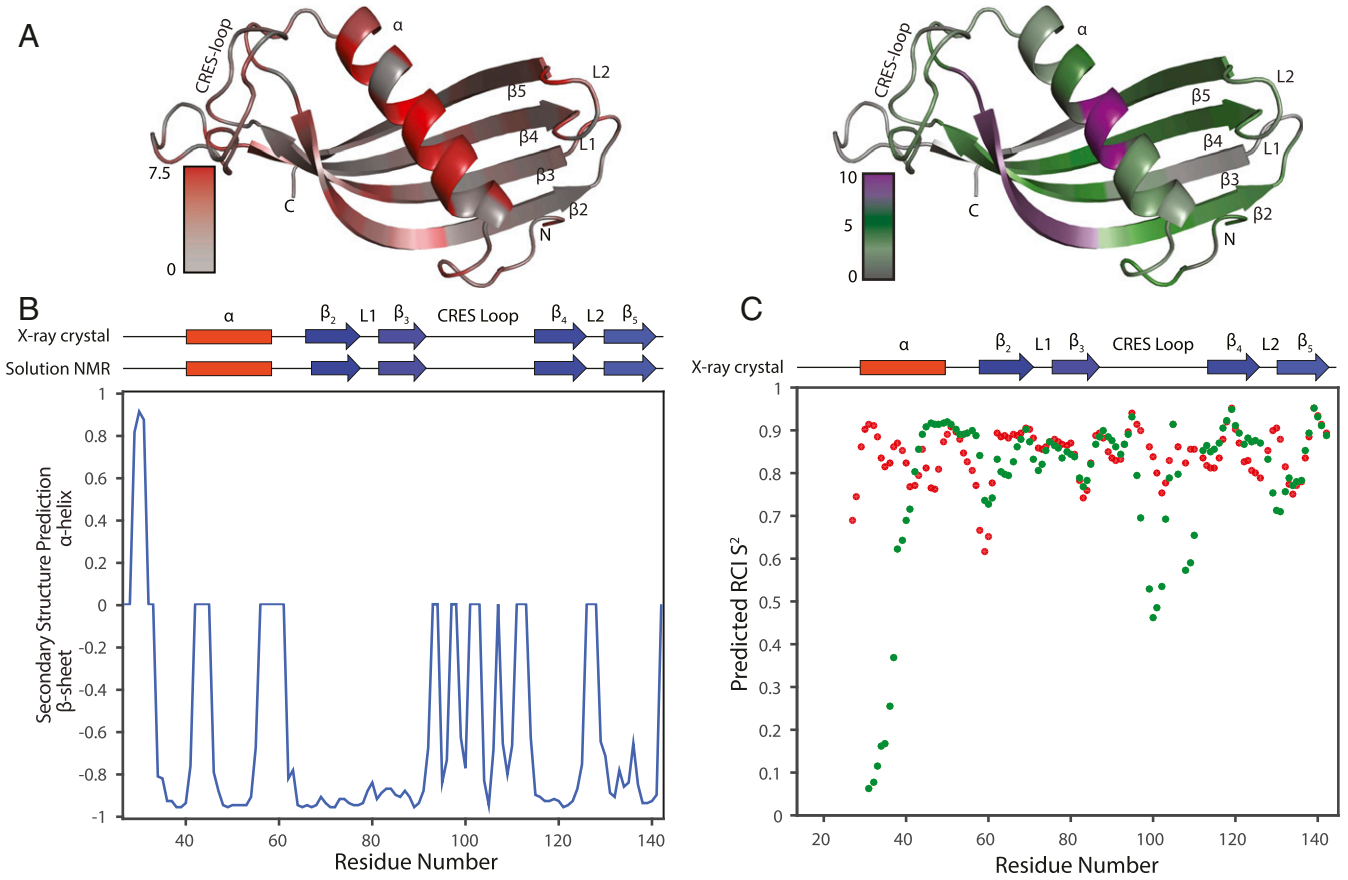

Fig. 5. Structural analysis of CRES using ssNMR chemical shift assignments. (*A*) The absolute value of CSPs between solid-state and solution-state NMR mapped onto solution-state NMR structure (shaded from gray to red) and AmylPred2 predicted amyloidogenic sites of the protein (shaded from gray [no prediction] to green [at least one prediction] to purple [unanimous prediction]). (*B*) Protein secondary structure predicted from ssNMR assigned chemical shifts using TALOS-N. Secondary structure components of CRES X-ray crystal structure and solution NMR are presented in red rectangles for α-helices and blue arrows for β-sheets. (*C*) Dot plot of predicted RCI S^2 from ssNMR (red) and solution NMR (green) chemical shifts.

other cystatins or could indicate this region stacks with other proteins analogously to many other reported amyloids. Our data also suggest β-sheet assemblies may occur through rigidification of the CRES loop. To generate possible structural models for the CRES amyloid, fragments were selected using the ssNMR chemical shift assignments and CS-ROSETTA and these were employed along with C2 symmetry in the ROSETTA fold-and-dock algorithm (40). While this model is dramatically underdetermined, it reveals key features which could help to explain the web-like, rather than fibrillar, structures observed via EM (Fig. 6*D*).

The lowest energy structural model in best agreement with the ssNMR chemical shifts is shown in Fig. 6*A* (in the *Top* panel each monomer is colored blue or yellow; below this, all residues predicted to be β-sheet by TALOS-N are highlighted in green). It is composed of six intra- and intermolecular β-strands as compared to five intramolecular β-strands found in the X-ray and solution NMR structures of monomeric CRES. In agreement with the TALOS-N analysis, CS-ROSETTA predicted the long α-helix is converted to a β-strand (residues A43 to E59) in the amyloid fold of the protein, and β2-L1-β3 form a long intermolecular strand, with this region of the first protomer forming an antiparallel sheet with the same region of the second (possibly reflective of domain swapping) (Fig. 6*A*). Another key feature predicted by this structure is that the amyloid matrix is composed of mostly antiparallel β-sheets rather than parallel β-sheets observed in many pathogenic amyloid structures. We previously reported CD and FTIR measurements indicative of antiparallel β-sheets in the early CRES aggregates (19). The ssNMR $^{13}C'$ chemical shifts reported here further support this conclusion in the advanced CRES amyloid. Backbone $^{13}C'$ chemical shifts are known to be highly sensitive to hydrogen bond length and geometry (41–44). Antiparallel β-sheets should have a slightly higher $^{13}C'$ chemical shift and narrower distribution (SD) compared to parallel β-sheets because their characteristic hydrogen bond lengths are slightly shorter, their bonding angles are more linear, and their overall registry is more ordered (45). Statistical comparison of the average and SD of $^{13}C'$ resonances found in CRES compared to a group of well-resolved parallel β-sheet amyloid structures (14, 15, 46–48) and well-established antiparallel globular proteins (49–52) (Fig. 6*B* and *SI Appendix*, Figs. S12 and S13), suggest the majority of β-sheets found in the CRES amyloid are antiparallel. Further justification is provided in *SI Appendix*. Lastly, the CRES loop in these CS-ROSETTA models is transitioning from its original random coil secondary structure toward a β-strand as predicted by TALOS-N. It does not transition completely to β-strand because within the limitations of the modeling software, which relies upon molecular symmetry, there is no packing partner.

It is unlikely the structure of the CRES amyloid matrix has any intrinsic symmetry. Although ssNMR suggests there may be a basic unit, which could be a domain-swapped core, the extensive β-sheet assemblies that may form via the CRES loop and other extremities of the model are likely not detected because they are

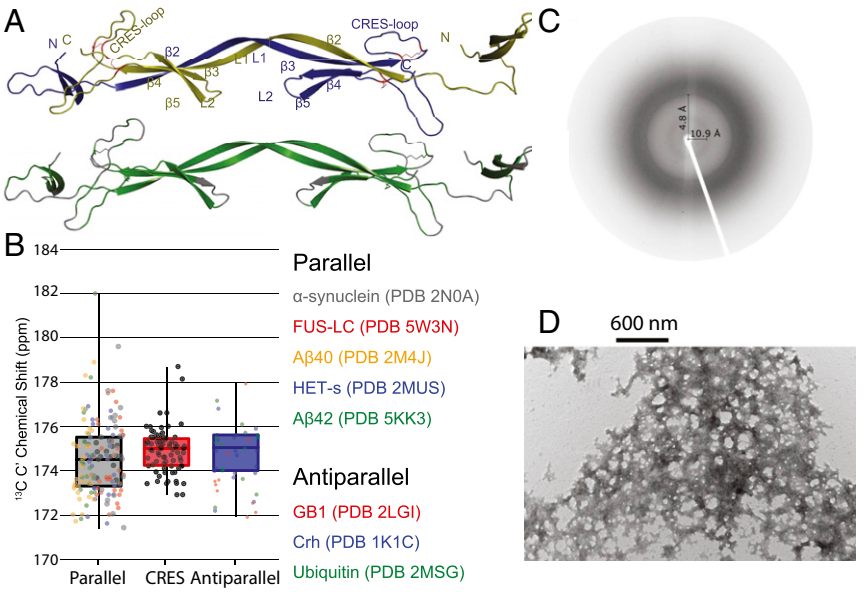

Fig. 6. Structural model of the CRES amyloid and X-ray diffraction and TEM images of advanced CRES amyloid matrix formed by the ssNMR sample. (*A*) Domain-swapped structures with monomeric units colored in blue and yellow (*Top*) and regions predicted to form β-sheets shaded in green (*Bottom*). Numbering of secondary structure is based on Fig. 1. (*B*) Comparison of average and SD of ^{13}C′ chemical shifts measured in advanced CRES amyloid compared to average and SD of well-defined parallel and antiparallel sheet structures. The dark horizontal line in each box signifies the average, the box signifies the 68% percent confidence interval, and the vertical line is the full spread of values. Color-coded dots are actual values reported for different proteins listed on the *Right*. (*C*) X-ray fiber diffraction of CRES amyloid matrix. X-ray fiber diffraction exhibited reflections at 4.8 Å and 10.9 Å, indicative of the spacing between β-strands and β-sheets, respectively. (*D*) Negative stain TEM image reveals a complicated web-like matrix formed by the CRES protein studied by ssNMR.

less frequent and are therefore not detectable in this ssNMR data. Indeed, there are multiple amyloid-prone contact surfaces branching out from the core of our model, implying extensive possibilities for the formation of intermolecular β-sheets. For example, the N terminus, CRES loop, β4, and β5 are capable of branching out from the core to form a complex matrix. In addition, multiple repeats of a β2-L1-β3 domain-swapped β-sheet could stack in a similar manner to fibrillar amyloids. It is thus possible that within the quaternary structure of the amyloid matrix, multiple intermolecular β-sheets could form along surfaces on multiple neighboring proteins. Consequently, as CRES aggregates, many of these β-strands intermingle, producing a far more complicated tertiary and quaternary structure. This β-sheet rich structure is further supported by X-ray fiber diffraction of the ssNMR sample (Fig. 6*C*), where the indicative 4.8-Å and 10.9-Å β-strand and β-sheet spacings are detected. The observation of multiple possible branch points is supported by negative stain transmission electron microscopy (TEM) images of the ssNMR sample (Fig. 6*D*). Similar to previously reported TEM images of both in vivo and in vitro samples, our CRES sample forms a webbed matrix (4, 18). Together, these data support the formation of an aggregated protein containing the β-sheet stacking characteristic of many amyloids, but uniquely prone toward antiparallel β-sheet secondary structures and a more complicated (nonfibrillar) quaternary organization.

Functional Amyloid Assembly. Our studies presented herein show at the atomic level the assembly of a functional mammalian amyloidogenic monomer to advanced amyloid. Using a combination of three powerful structural biology techniques, we not only reveal the structure of the CRES monomer and its advanced amyloid form but provide critical knowledge of how a biological amyloidogenic precursor initiates its assembly into early oligomeric forms under physiological conditions. Together, our data suggest that CRES amyloid formation is complex and likely utilizes several mechanisms, including a unique interaction driven by changes in the structure of a CRES loop from a flexible linker in the monomer to a β-strand conformation in the advanced amyloid as well as traditional domain swapping typical of other cystatins. We speculate that one role of the CRES loop may be to guide and control the building of highly branched and elaborate amyloid matrices whose β-sheet assemblies with neighboring proteins, including other amyloidogenic precursors, may be essential for biological function. Indeed, early mutagenesis studies in which three asparagine and one threonine residue in the CRES loop were replaced with alanine residues revealed a monomer that no longer polymerized into a metastable oligomer typical of wild-type CRES but rather which rapidly progressed to large aggregates suggestive of an uncontrolled amyloid assembly process (19) (*SI Appendix*, Fig. S14). Structural heterogeneity, including lateral attachments, from a basic structural unit has also been observed in the fungal hydrophobin $EAS_{\Delta 15}$ amyloid, a functional truncated variant which forms an extended amphipathic monolayer at hydrophobic:hydrophilic interfaces (53). Based on mutagenesis experiments and docking models, a highly mobile, disulfide-anchored, and asparagine-rich loop was proposed to be central to the conformational transition of EAS to its antiparallel β-sheet-rich amyloid form (54). The intriguing similarity of this model with our demonstrated role of the CRES loop in mammalian amyloid assembly suggests that rigidification of a flexible loop may be an evolutionarily conserved mechanism for the controlled assembly of some functional amyloids. The use of multiple assembly mechanisms could also allow functional amyloids to adopt very different geometries if one mechanism dominated over the other, which could be mediated by local environmental conditions. Further, the use of distinctive mechanisms to assemble amyloid within a common structure could also be a means to selectively disassemble specific β-sheet interactions allowing a highly dynamic and plastic functional amyloid structure.

Materials and Methods

Protein Expression and Purification. Tag-less CRES C48A was purified from the soluble fraction of bacteria using affinity, ion exchange, and gel filtration

chromatography as previously described (19). Mass spectra of intact and tryptic digests of CRES isoforms were acquired using a matrix-assisted laser desorption/ionization time of flight (MALDI-TOF/TOF) 4800 mass spectrometer (Applied Biosystems) as detailed in *SI Appendix*.

X-ray Crystallization. CRES C48A crystals were grown using the hanging drop method and shipped to the Stanford Linear Accelerator Center (SLAC) beamline 7–1 for high-resolution data collection. The structure was solved as detailed in *SI Appendix*.

Solution-State and Magic-Angle Spinning Solid-State NMR. All solution-state NMR data were recorded on a 600 MHz (^{1}H Larmor frequency; 14 T) Agilent DD2 spectrometer equipped with a *z* axis gradient room temperature ^{1}H-^{13}C-^{15}N (HCN) probe. Solid-state NMR experiments were carried out on a 600-MHz Agilent DD2 three-channel spectrometer equipped with an HCN Baun probe. Details are provided in *SI Appendix*.

Negative Stain TEM. CRES C48A was spotted on to formvar/carbon-coated 200 mesh nickel grids (Ted Pella) as described (4).

Data Availability. The atomic coordinates and structure factors have been deposited in the Protein Data Bank, www.rcsb.org (PDB ID code 6UIO) (55). Solution-state NMR data ID 50273 (56) and solid-state NMR data ID 50275 (57) have been deposited in the Biological Magnetic Resonance Bank.

ACKNOWLEDGMENTS. We thank Masoud Zabet of the Texas Tech University (TTU) Proteomics core for the mass spectrophotometric analysis of CRES isoforms and the preparation of *SI Appendix*, Fig. S1*B*. We acknowledge the High Performance Computing (HPC) Center at TTU at Lubbock for providing HPC resources that have contributed to the research results reported within this paper (www.depts.ttu.edu/hpcc/). Use of the Stanford Synchrotron Radiation Lightsource (SSRL), SLAC National Accelerator Laboratory, is supported by the US Department of Energy (DOE), Office of Science, Office of Basic Energy Sciences under Contract DE-AC02-76SF00515. The SSRL Structural Molecular Biology Program is supported by the DOE Office of Biological and Environmental Research, and by the National Institutes of Health, National Institute of General Medical Sciences (NIGMS) (P41GM103393). The contents of this publication are solely the responsibility of the authors and do not necessarily represent the official views of NIGMS or NIH. This work was supported by TTU Health Sciences Center; the Wilson Foundation; the Newby Family (G.A.C.); and NIH Grants R01AR063634 (R.B.S.), 1R35GM128906 (M.P.L.), and 1R35GM124979 (B.J.W.).

1. D. M. Fowler *et al*., Functional amyloid formation within mammalian tissue. *PLoS Biol.* **4**, e6 (2006).
2. E. Boke *et al*., Amyloid-like self-assembly of a cellular compartment. *Cell* **166**, 637–650 (2016).
3. B. L. Raveendra *et al*., Characterization of prion-like conformational changes of the neuronal isoform of Aplysia CPEB. *Nat. Struct. Mol. Biol.* **20**, 495–501 (2013).
4. S. Whelly *et al*., Nonpathological extracellular amyloid is present during normal epididymal sperm maturation. *PLoS One* **7**, e36394 (2012).
5. N. R. Roan *et al*., Semen amyloids participate in spermatozoa selection and clearance. *eLife* **6**, e24888 (2017).
6. B. Guyonnet, N. Egge, G. A. Cornwall, Functional amyloids in the mouse sperm acrosome. *Mol. Cell. Biol.* **34**, 2624–2634 (2014).
7. N. Egge, A. Muthusubramanian, G. A. Cornwall, Amyloid properties of the mouse egg zona pellucida. *PLoS One* **10**, e0129907 (2015).
8. S. K. Maji *et al*., Functional amyloids as natural storage of peptide hormones in pituitary secretory granules. *Science* **325**, 328–332 (2009).
9. C. M. Pfefferkorn, R. P. McGlinchey, J. C. Lee, Effects of pH on aggregation kinetics of the repeat domain of a functional amyloid, Pmel17. *Proc. Natl. Acad. Sci. U.S.A.* **107**, 21447–21452 (2010).
10. S. Whelly *et al*., Cystatin-related epididymal spermatogenic subgroup members are part of an amyloid matrix and associated with extracellular vesicles in the mouse epididymal lumen. *Mol. Hum. Reprod.* **22**, 729–744 (2016).
11. A. W. P. Fitzpatrick *et al*., Cryo-EM structures of tau filaments from Alzheimer's disease. *Nature* **547**, 185–190 (2017).
12. N. L. Fawzi, J. Ying, R. Ghirlando, D. A. Torchia, G. M. Clore, Atomic-resolution dynamics on the surface of amyloid-β protofibrils probed by solution NMR. *Nature* **480**, 268–272 (2011).
13. M. A. Wälti *et al*., Atomic-resolution structure of a disease-relevant Aβ(1-42) amyloid fibril. *Proc. Natl. Acad. Sci. U.S.A.* **113**, E4976–E4984 (2016).
14. M. T. Colvin *et al*., Atomic resolution structure of monomorphic Aβ42 amyloid fibrils. *J. Am. Chem. Soc.* **138**, 9663–9674 (2016).
15. D. T. Murray *et al*., Structure of FUS protein fibrils and its relevance to self-assembly and phase separation of low-complexity domains. *Cell* **171**, 615–627.e16 (2017).
16. M. Mompeán *et al*., The structure of the necrosome RIPK1-RIPK3 core, a human hetero-amyloid signaling complex. *Cell* **173**, 1244–1253.e10 (2018).
17. H. Van Melckebeke *et al*., Atomic-resolution three-dimensional structure of HET-s(218-289) amyloid fibrils by solid-state NMR spectroscopy. *J. Am. Chem. Soc.* **132**, 13765–13775 (2010).
18. G. A. Cornwall, H. Q. Do, A. Hewetson, A. Muthusubramanian, C. Myers, The epididymal amyloid matrix: Structure and putative functions. *Andrology* **7**, 603–609 (2019).
19. H. Q. Do *et al*., The functional mammalian CRES (Cystatin-Related epididymal spermatogenic) amyloid is antiparallel β-Sheet rich and forms a metastable oligomer during assembly. *Sci. Rep.* **9**, 9210 (2019).
20. R. Kolodziejczyk *et al*., Crystal structure of human cystatin C stabilized against amyloid formation. *FEBS J.* **277**, 1726–1737 (2010).
21. J. Bibby, R. M. Keegan, O. Mayans, M. D. Winn, D. J. Rigden, AMPLE: A cluster-and-truncate approach to solve the crystal structures of small proteins using rapidly computed ab initio models. *Acta Crystallogr. D Biol. Crystallogr.* **68**, 1622–1631 (2012).
22. M. Maszota-Zieleniak *et al*., (NMR and crystallographic structural studies of the extremely stable monomeric variant of human cystatin C with single amino acid substitution. *FEBS J.* **287**, 361–376 (2020).
23. R. Janowski, M. Kozak, M. Abrahamson, A. Grubb, M. Jaskolski, 3D domain-swapped human cystatin C with amyloidlike intermolecular beta-sheets. *Proteins* **61**, 570–578 (2005).
24. J. Ghiso, O. Jensson, B. Frangione, Amyloid fibrils in hereditary cerebral hemorrhage with amyloidosis of Icelandic type is a variant of gamma-trace basic protein (cystatin C). *Proc. Natl. Acad. Sci. U.S.A.* **83**, 2974–2978 (1986).
25. M. Orlikowska, E. Jankowska, R. Kołodziejczyk, M. Jaskólski, A. Szymańska, Hinge-loop mutation can be used to control 3D domain swapping and amyloidogenesis of human cystatin C. *J. Struct. Biol.* **173**, 406–413 (2011).
26. E. Dall *et al*., Structural and functional analysis of cystatin E reveals enzymologically relevant dimer and amyloid fibril states. *J. Biol. Chem.* **293**, 13151–13165 (2018).
27. G. A. Cornwall *et al*., The cystatin-related epididymal spermatogenic protein inhibits the serine protease prohormone convertase 2. *Endocrinology* **144**, 901–908 (2003).
28. C. M. Wilmot, J. M. Thornton, Analysis and prediction of the different types of beta-turn in proteins. *J. Mol. Biol.* **203**, 221–232 (1988).
29. W. Kabsch, C. Sander, Dictionary of protein secondary structure: Pattern recognition of hydrogen-bonded and geometrical features. *Biopolymers* **22**, 2577–2637 (1983).
30. E. Krissinel, K. Henrick, Inference of macromolecular assemblies from crystalline state. *J. Mol. Biol.* **372**, 774–797 (2007).
31. Y. Shen, A. Bax, Protein backbone and sidechain torsion angles predicted from NMR chemical shifts using artificial neural networks. *J. Biomol. NMR* **56**, 227–241 (2013).
32. M. V. Berjanskii, D. S. Wishart, A simple method to predict protein flexibility using secondary chemical shifts. *J. Am. Chem. Soc.* **127**, 14970–14971 (2005).
33. R. Powers, G. M. Clore, D. S. Garrett, A. M. Gronenborn, Relationships between the precision of high-resolution protein NMR structures, solution-order parameters, and crystallographic B-factors. *J. Magn. Reson. B.* **101**, 325–327 (1993).
34. V. A. Jarymowycz, M. J. Stone, Fast time scale dynamics of protein backbones: NMR relaxation methods, applications, and functional consequences. *Chem. Rev.* **106**, 1624–1671 (2006).
35. A. Sekhar, L. E. Kay, NMR paves the way for atomic level descriptions of sparsely populated, transiently formed biomolecular conformers. *Proc. Natl. Acad. Sci. U.S.A.* **110**, 12867–12874 (2013).
36. M. R. Palmer *et al*., Sensitivity of nonuniform sampling NMR. *J. Phys. Chem. B* **119**, 6502–6515 (2015).
37. R. Amani *et al*., Conformational changes upon gating of KirBac1.1 into an open-activated state revealed by solid-state NMR and functional assays. *Proc. Natl. Acad. Sci. U.S.A.* **117**, 2938–2947 (2020).
38. R. Janowski *et al*., Human cystatin C, an amyloidogenic protein, dimerizes through three-dimensional domain swapping. *Nat. Struct. Biol.* **8**, 316–320 (2001).
39. A. C. Tsolis, N. C. Papandreou, V. A. Iconomidou, S. J. Hamodrakas, A consensus method for the prediction of 'aggregation-prone' peptides in globular proteins. *PLoS One* **8**, e54175 (2013).
40. R. Das *et al*., Simultaneous prediction of protein folding and docking at high resolution. *Proc. Natl. Acad. Sci. U.S.A.* **106**, 18978–18983 (2009).
41. B. J. Wylie *et al*., Chemical-shift anisotropy measurements of amide and carbonyl resonances in a microcrystalline protein with slow magic-angle spinning NMR spectroscopy. *J. Am. Chem. Soc.* **129**, 5318–5319 (2007).
42. Y. Wei, D. K. Lee, A. Ramamoorthy, Solid-state (13)C NMR chemical shift anisotropy tensors of polypeptides. *J. Am. Chem. Soc.* **123**, 6118–6126 (2001).
43. T. Kameda *et al*., Hydrogen-bonded structure and C-13 NMR chemical shift tensor of amino acid residue carbonyl carbons of peptides and polypeptides in the crystalline state. 1. *J. Mol. Struct.* **384**, 17–23 (1996).
44. T. Kameda, I. Ando, The relationship between the helical conformation and C-13 NMR chemical shift of amino acid residue carbonyl carbons of polypeptides in the solid state. *J. Mol. Struct.* **412**, 197–203 (1997).

45. L. Pauling, R. B. Corey, The pleated sheet, a new layer configuration of polypeptide chains. *Proc. Natl. Acad. Sci. U.S.A.* **37**, 251–256 (1951).
46. M. D. Tuttle *et al*., Solid-state NMR structure of a pathogenic fibril of full-length human α-synuclein. *Nat. Struct. Mol. Biol.* **23**, 409–415 (2016).
47. J. X. Lu *et al*., Molecular structure of β-amyloid fibrils in Alzheimer's disease brain tissue. *Cell* **154**, 1257–1268 (2013).
48. C. Wasmer *et al*., Amyloid fibrils of the HET-s(218-289) prion form a beta solenoid with a triangular hydrophobic core. *Science* **319**, 1523–1526 (2008).
49. B. J. Wylie *et al*., Ultrahigh resolution protein structures using NMR chemical shift tensors. *Proc. Natl. Acad. Sci. U.S.A.* **108**, 16974–16979 (2011).
50. T. I. Igumenova *et al*., Assignments of carbon NMR resonances for microcrystalline ubiquitin. *J. Am. Chem. Soc.* **126**, 6720–6727 (2004).
51. T. I. Igumenova, A. J. Wand, A. E. McDermott, Assignment of the backbone resonances for microcrystalline ubiquitin. *J. Am. Chem. Soc.* **126**, 5323–5331 (2004).
52. H. K. Fasshuber *et al*., Structural heterogeneity in microcrystalline ubiquitin studied by solid-state NMR. *Protein Sci.* **24**, 592–598 (2015).
53. V. K. Morris *et al*., Solid-state NMR spectroscopy of functional amyloid from a fungal hydrophobin: A well-ordered β-sheet core amidst structural heterogeneity. *Angew. Chem. Int. Ed. Engl.* **51**, 12621–12625 (2012).
54. I. Macindoe *et al*., Self-assembly of functional, amphipathic amyloid monolayers by the fungal hydrophobin EAS. *Proc. Natl. Acad. Sci. U.S.A.* **109**, E804–E811 (2012).
55. M. J. Dominguez, G. A. Cornwall, A. Hewetson, R. B. Sutton, Crystal structure of mouse CRES (cystatin-related epididymal spermatogenic). Protein Data Bank. 10.2210/pdb6UIO/pdb. Deposited 30 September 2019.
56. N. H. Khan, M. P. Latham, Solution-state NMR. Maturation of the functional mouse CRES amyloid from globular form. Biological Magnetic Resonance Bank. http://deposit.bmrb.wisc.edu/author_view/BMRB/50273_hy_gurasfsk.str. Deposited 14 May 2020.
57. N. H. Khan, C. G. Borcik, B. J. Wylie. Solid-state NMR. Maturation of the functional mouse CRES amyloid from globular form. Biological Magnetic Resonance Bank. http://deposit.bmrb.wisc.edu/author_view/BMRB/50275_hy_svgtujyb.str. Deposited 14 May 2020.